ChemComm

COMMUNICATION

View Article Online
View Journal | View Issue

Cite this: *Chem. Commun.*, 2020, **56**, 2415

Received 7th January 2020,
Accepted 16th January 2020

DOI: 10.1039/d0cc00142b

rsc.li/chemcomm

Hydrophilic polyphosphoester-conjugated fluorinated chlorin as an entirely biodegradable nano-photosensitizer for reliable and efficient photodynamic therapy†

Zhiyong Liu,[a] Mengsi Wu,[a] Yudong Xue,[a] Chao Chen,[b] Frederik R. Wurm,*[c] Minbo Lan[a] and Weian Zhang*[a]

An entirely biodegradable nano-photosensitizer platform (PPE-FP$_2$) was fabricated by conjugating the photosensitizer TFPC to hydrophilic polyphosphoesters (PPEs) for efficiently liberating photosensitizers at the tumor site. The complete biodegradability of PPE-FP$_2$ avoided residual nanoparticles *in vivo* after therapy, realizing reliable and effective photodynamic therapy.

Nanocarriers such as liposomes,[1,2] polymer micelles,[3,4] MOFs[5–7] and inorganic nanoparticles[8,9] have been fabricated to deliver drugs to tumor cells *via* the enhanced permeability and retention (EPR) effect.[10,11] In particular, pegylated nanoparticles have received massive attention. However, PEG cannot be biodegraded *in vivo*. Several concerns associated with the non-biodegradability of PEG have been raised, especially for long-term administration.[12] The accumulation of PEG *in vivo* has been reported to result in intracellular vacuolation of organs such as the renal tubules, due to the stability of PEG.[13] Furthermore, the formation of PEG antibodies has been observed, which can induce immune responses and accelerate the clearance of nanoparticles modified by PEG.[14] To address the defects of non-biodegradable PEG, novel stealth polymers such as polyphosphoesters (PPEs),[15] and also zwitterionic polymers,[16–18] hydroxyethyl starch[19,20] or dextrin[21] have been proposed.

PPEs present great potential as a stealth material due to their biocompatibility and biodegradability.[22] The backbone of PPEs is similar to biomacromolecules, such as DNA, RNA and teichoic acids and phosphorus is a fundamental element of bone making up 1% of the total human body mass.[23,24] Therefore, the final degradation products of PPEs, phosphate or phosphonate, exist in or are well tolerated by the human body. Moreover, the backbone of PPEs can be cleaved under physiological conditions or recognized by enzymes, such as alkaline phosphatase, which is increased in tumor cells and can accelerate the hydrolysis of PPEs.[25,26] Furthermore, the hydrolysis rate and functionality of PPEs can be controlled by side chain attachment resulting from reactive pendant groups of pentavalent phosphorus.[27] Based on PPEs, Wooley *et al.* have designed several types of micelles used for drug delivery and gene therapy.[28,29] In addition, Wang *et al.* also reported PPE-based nanoparticles for improving the anti-tumor effect of drugs.[30,31] Importantly, as a stealth biomaterial, hydrophilic PPE has been verified to reduce protein adsorption and prevent nonspecific cellular uptake as well as PEG.[32] Consequently, an effective and secure therapy could be achieved by a direct conjugation of PPE with hydrophobic agents.

Herein, we developed a fully biodegradable polymer photosensitizer by conjugating 7,8-dihydro-5,10,15,20-tetrakis(pentafluorophenyl)-21*H*,23*H*-porphine (TFPC) to the hydroxyl end groups of a telechelic poly(methyl ethylene phosphate) (PPE) as shown in Scheme 1. PPE is a hydrophilic polymer and after conjugation will self-assemble into larger aggregates with a PPE shell that should reduce protein adsorption. TFPC as a hydrophobic macrocyclic aromatic compound is easy to aggregate through π–π stacking and hydrophobic interaction; therefore, the polymer-photosensitizer conjugate can assemble into nanoparticles and accumulate in tumor sites by the EPR effect. Moreover, PPEs can be degraded in a physiological environment or by phosphatase, thus TFPC could be released from the nanoparticles for enhancing the sensitivity of photosensitizers to oxygen. Furthermore, the degradation of the nanoparticles can avoid their *in vivo* accumulation after therapy, reducing the side effects.

Meso-tetrakis(pentafluorophenyl)porphyrin (TFPP) was synthesized and then reduced by *p*-toluenesulfonylhydrazide to obtain the red-light-absorbing photosensitizer TFPC as shown in Scheme S1 (ESI†). Di-hydroxyl functionalized PPE with a molar mass of 4000 g mol^{-1} was synthesized by anionic ring-opening polymerization by an adapted literature protocol as the stealth material.[33] **PPE-FP$_2$** was prepared by conjugation of TFPC to

[a] *Shanghai Key Laboratory of Functional Materials Chemistry, East China University of Science and Technology, 130 Meilong Road, Shanghai 200237, China. E-mail: wazhang@ecust.edu.cn*

[b] *State Key Laboratory of Bioreactor Engineering Center, East China University of Science and Technology, 130 Meilong Road, Shanghai 200237, China*

[c] *Max Planck Institute for Polymer Research, Ackermannweg 10, Mainz 55128, Germany. E-mail: wurm@mpip-mainz.mpg.de*

† Electronic supplementary information (ESI) available. See DOI: 10.1039/d0cc00142b

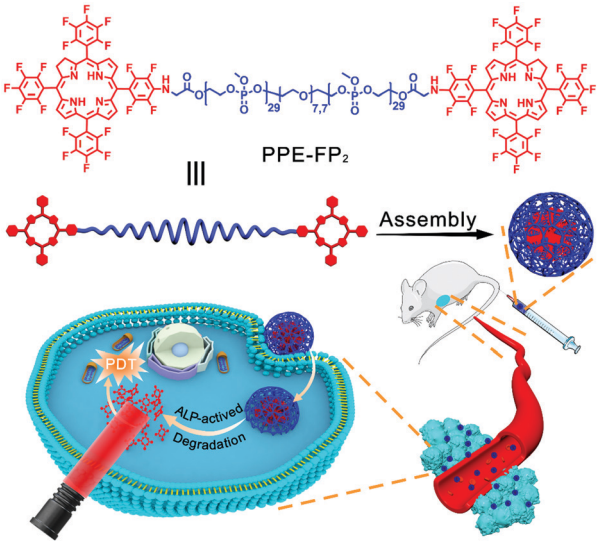

Scheme 1 Schematic illustration of the self-assembly and application in photodynamic therapy of **PPE-FP$_2$**.

PPE *via* esterification as shown in Scheme S1 (ESI†) and further assembled into spherical nanoparticles. Additionally, the PEG-analog, **PEG-FP$_2$** (Scheme S2, ESI†) was also prepared *via* a similar approach as a non-degradable control (detailed characterization is given in Fig. S1–S11, ESI†). Both polymer conjugates, **PPE-FP$_2$** and **PEG-FP$_2$** could be dispersed well in water and by the naked eye generated a stable dispersion with the typical yellowish color of the chlorin. In contrast, hydrophobic TFPC remained insoluble and sedimented. For both **PPE-FP$_2$** and **PEG-FP$_2$**, spherical nanoparticles could be observed after the self-assembly by transmission electron microscopy (TEM) images (Fig. 1b and c). The size of the nanoparticles was relatively uniform for both **PPE-FP$_2$** and **PEG-FP$_2$** with average diameters of *ca.* 100 nm and 110 nm, respectively. Dynamic light scattering (DLS) further confirmed the size of the nanoparticles and supported the relatively narrow size distribution (Fig. 1d, an average hydrodynamic size of 160 nm, which is slightly larger than that determined by TEM, probably due to hydration). Subsequently, the potentials for photodynamic therapy and fluorescence imaging of **PPE-FP$_2$** were evaluated by UV absorbance spectrum in Fig. 1e and fluorescence emission spectroscopy in Fig. 1f, which show that **PPE-FP$_2$** nanoparticles have strong absorption (655 nm, $\varepsilon_{(TFPC)}$ = 1.62 × 10^4 L (mol^{-1} cm^{-1})) and emission (600–750 nm) in the far-red light region; therefore, **PPE-FP$_2$** nanoparticles could be used as a potential agent for the diagnosis of solid tumors.

The *in vitro* biodegradability of the **PPE-FP$_2$** conjugate was separately assessed after direct dispersion in phosphate-buffered saline at pH = 7.4 and after the addition of alkaline phosphatase (ALP) while being shaken on a horizontal shaker at 37 °C. It is known that the concentration of ALP is increased in tumor cells, which should lead to an accelerated degradation of PPE.[25] The degradation of **PPE-FP$_2$** in PBS with or without ALP was proven by UV absorbance and DLS measurements after certain time intervals (Fig. 2a–e and Fig. S12 and S13, ESI†). Compared with dispersion in PBS without ALP, the degradation rate of **PPE-FP$_2$** nanoparticles increased significantly in the presence of ALP, resulting in greater absorption reduction during 24 h as shown in Fig. 2b and c, which would promote photosensitizers to be effectively released from the **PPE-FP$_2$** nanoparticles at tumor sites. Degradation was followed by DLS (as shown in Fig. 2d and e and Fig. S13, ESI†): the size distribution of **PEG-FP$_2$** nanoparticles remained nearly unchanged, as they remained hydrolytically stable under these conditions, while the colloidal stability of the degradation products from **PPE-FP$_2$** decreased as the PPE hydrolyzed, resulting in aggregation of the hydrophobic chlorin. In the presence of ALP, **PPE-FP$_2$** nanoparticles were quickly destabilized during the first day, which further proved the biodegradation behavior of PPE accelerated by ALP. TEM images shown in Fig. S14–S18 (ESI†) also demonstrated that **PPE-FP$_2$** nanoparticles without the presence of ALP could maintain their distribution during the first day and degrade to irregular assembled aggregates after 3 days.

Reactive oxygen species (ROS) generation of the nanoparticles was confirmed by using 1,3-diphenylisobenzofuran (DPBF) as an ROS indicator before investigating the *in vitro* and *in vivo* PDT performance.[34] ROS generated by nanoparticles

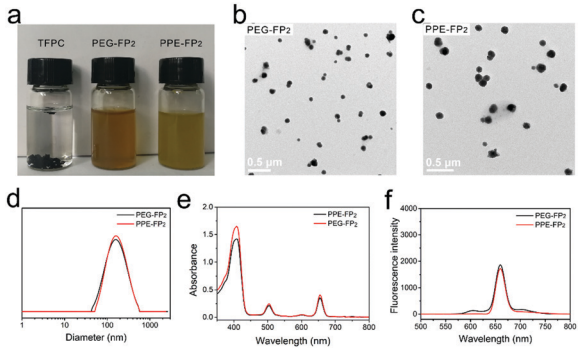

Fig. 1 Characterization of **PEG-FP$_2$** and **PPE-FP$_2$** nanoparticles. (a) Photographs of TFPC, **PEG-FP$_2$** and **PPE-FP$_2$** in water. (b and c) TEM images of **PEG-FP$_2$** and **PPE-FP$_2$** nanoparticles. (d) Dynamic light scattering data of the nanoparticles. (e) UV spectra and (f) fluorescence spectra (ex: 425 nm) in ultrapure water.

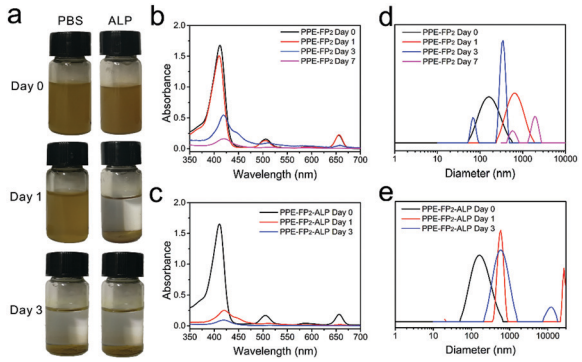

Fig. 2 Stability evaluation of **PPE-FP$_2$** under different conditions. (a) Photos taken from the dispersions over time. UV spectrum of **PPE-FP$_2$** dispersed in PBS (b) and PBS with ALP (c). (d and e) Size distribution determined by DLS.

under 655 nm laser irradiation were recorded by a decrease of characteristic absorption of DPBF at *ca.* 415 nm (Fig. S19, ESI†). This result proved that both **PPE-FP$_2$** and **PEG-FP$_2$** nanoparticles could be used to as antitumor agents in PDT.

Confocal laser scanning microscopy (CLSM) was used to determine the cellular uptake of the nanoparticles. As shown in Fig. 3a, both **PPE-FP$_2$** and **PEG-FP$_2$** nanoparticles could be taken up effectively after incubating with 4T1 cells for 24 h. Interestingly, the fluorescence intensity of the cells treated with **PPE-FP$_2$** after 24 h was higher than that of the cells incubated with **PEG-FP$_2$**, which might be a result of the degradation of **PPE-FP$_2$** after internalization into the tumor cells. Flow cytometry was used to study the cellular uptake of the chlorin conjugates (Fig. S20, ESI†). Gradually enhanced intracellular fluorescence intensity was observed with prolonged incubation times for both **PPE-FP$_2$** and **PEG-FP$_2$**, indicating efficient internalization of the nanoparticles. Specifically, we found that the curves of fluorescence intensity of **PPE-FP$_2$** had two peaks at 4 h while there was only one peak at 24 h, indicating that PPE could be gradually degraded. Moreover, the higher fluorescence intensity of TFPC was observed in tumor cells treated with **PPE-FP$_2$** compared with cells incubated with **PEG-FP$_2$**. These results suggested that **PPE-FP$_2$** could be gradually degraded to release TFPC in cells, thus reducing the aggregation induced quenching effect, which might enhance the PDT effect.

To gain insight into the PDT ability of **PPE-FP$_2$**, the intracellular ROS generation of **PPE-FP$_2$** was evaluated by using 2,7-dichlorofluorescein diacetate (DCFH-DA) as an ROS probe.[35] As shown in Fig. 3b, when combined with laser irradiation, the green fluorescence intensity of **PPE-FP$_2$** was significantly increased compared to that of the control, while **PEG-FP$_2$** exhibited a moderate enhancement of fluorescence. This result indicated the mass production of intracellular ROS induced by the nanoparticles under 655 nm laser irradiation, especially for biodegradable **PPE-FP$_2$**. Based on these results, the *in vitro* PDT effect against 4T1 cells was verified *via* MTT assay. The cell viability approved in Fig. 3c demonstrated that **PPE-FP$_2$** and **PEG-FP$_2$** both have no significant cytotoxicity without laser irradiation on account of their good biocompatibility. However, when the cells incubated with nanoparticles were irradiated with a 655 nm laser, the cell viability showed a prominent decrease with the increase of the concentration of nanoparticles. Moreover, **PPE-FP$_2$** (IC_{50}: 24 μg mL^{-1}, calculated for chlorin concentration) exhibited a more efficient therapeutic effect than **PEG-FP$_2$** (IC_{50}: 42 μg mL^{-1}), which may have resulted from the biodegradation of **PPE-FP$_2$** accompanied by the liberation of TFPC.

Near infrared fluorescence agent Cyanine 7 (Cy7), a fluorescence quenching agent of TFPC based on fluorescence resonance energy transfer (FRET),[36] was co-assembled with **PPE-FP$_2$** for *in vivo* fluorescence imaging as shown in Fig. 4a. The successful encapsulation of Cy7 is determined by UV spectra and DLS (Fig. S21 and S22, ESI†). The fluorescence imaging monitored in real-time revealed that nanoparticles could gradually accumulate into the tumor site with the extension of time and show a strong fluorescence signal at the tumor site at 24 h post-injection (p.i.). This consequence demonstrated that nanoparticles could effectively deliver TFPC into the tumor site through the EPR effect.

Encouraged by the remarkable previous consequences, 4T1-tumor-bearing mice were used to investigate the *in vivo* anti-tumor performance. The mice were randomly divided into five groups: control, **PEG-FP$_2$**, **PPE-FP$_2$**, **PEG-FP$_2$** + **L** (655 nm laser irradiation), and **PPE-FP$_2$** + **L**. Relative tumor volume was recorded to study the suppressive effect as shown in Fig. 4b. The **PEG-FP$_2$** + **L** and **PPE-FP$_2$** + **L** groups showed a remarkable delay in tumor growth or tumor regression as compared with the control groups after 18 days. To further underline the

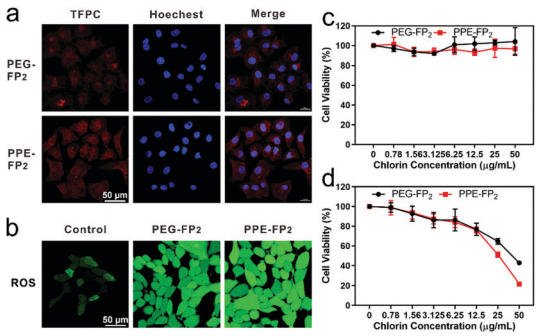

Fig. 3 Intracellular distribution and *in vitro* photodynamic therapy. CLSM images of (a) endocytosis by 4T1 cells and (b) intracellular ROS detected by DCFH-DA as a fluorescent probe. Cell viability against 4T1 cells (c) without and (d) with 655 nm laser (100 mW cm^{-2}, 10 min) evaluated by MTT assay after incubation with **PEG-FP$_2$** and **PPE-FP$_2$** for 24 h.

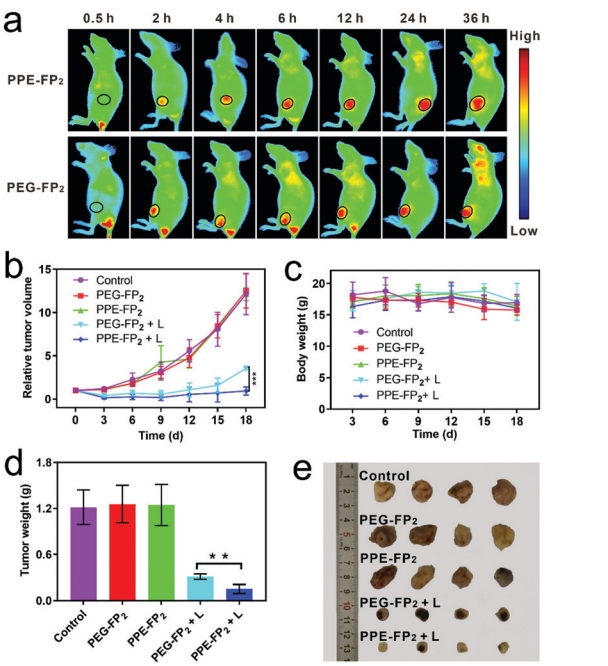

Fig. 4 *In vivo* fluorescence imaging and anti-tumor efficacy against 4T1 tumors after intravenous injection of PBS (control), **PEG-FP$_2$** and **PPE-FP$_2$** nanoparticles at a TFPC-equivalent dose of 1 mg kg^{-1}. (a) Cy7 (ex: 700 nm, em: 780 nm). (b) Relative tumor volumes. (c) Body weight and (d) tumor weight and (e) photographs of tumors. (n = 4, mean ± s.d., $^{**}P < 0.01$, $^{***}P < 0.001$).

efficiency of phototherapy, the tumors were excised from the mice and weighed to obtain the accurate tumor weight after the mice were sacrificed on day 18. As shown in Fig. 4d and e, tumors irradiated by a laser successfully reduced the size and weight, indicating the efficient photodynamic anti-tumor effect of **PPE-FP$_2$** and **PEG-FP$_2$**. Besides, we found that there is a slow growth trend for tumors in the **PEG-FP$_2$** + **L** group while no obvious change in the **PPE-FP$_2$** + **L** group was observed, which could be attributed to the biodegradation behavior of **PPE-FP$_2$** with the enhanced PDT efficacy. Qualitative histological examinations were also carried out by hematoxylin and eosin (H&E) staining of tumor slices (Fig. S23, ESI†). Significant necrosis was observed on groups irradiated with a laser, especially for the **PPE-FP$_2$** + **L** group, proving the evident destruction of tumor cells by phototherapy. Fig. 4c and Fig. S24 (ESI†) revealed the minimal side effects of **PEG-FP$_2$** and **PPE-FP$_2$** during treatment.

A major benefit of PPE is the hydrolytic lability; thus, we increased the dose of the chlorin conjugates. The mice were sacrificed after two months, and then the kidneys and spleens were harvested and stained by H&E for toxicity analysis. Fig. S25 (ESI†) revealed that the kidneys, and spleens of mice administered with **PEG-FP$_2$** were damaged distinctly. In contrast, those treated with **PPE-FP$_2$** showed almost no damage. These results could be attributed to the degradation of PPEs avoiding the long-term accumulation of nanoparticles in the organs, indicating that the biodegradability of PPE endowed **PPE-FP$_2$** with excellent biological safety.

In summary, by conjugating TFPC to PPE, we developed a biodegradable nano-photosensitizer (**PPE-FP$_2$**) for safe and effective photodynamic therapy. **PPE-FP$_2$** can be assembled into spherical nanoparticles and accumulate in tumor cells *via* the EPR effect. In addition, benefiting from the effective far-red absorption, **PPE-FP$_2$** could achieve deep tumor penetration. Importantly, as **PPE-FP$_2$** could be degraded, TFPC can be released from the assembly after cellular uptake, increasing the photodynamic efficacy of the PPE-conjugates, compared to the non-degradable PEGylated analog. In addition, as **PPE-FP$_2$** can be degraded and did not show any cytotoxicity in the absence of light, long-term *in vivo* accumulation is prevented. We believe that the nano-photosensitizers based on PPE are a new platform to design safe and more efficient photodynamic therapies. Together with the potential chemical functionality of PPEs, further targeting ligands or variation in their biodegradation profile can be installed, which will be studied in future projects.

This work was financially supported by the National Natural Science Foundation of China (No. 21875063), and the Open Access funding provided by the Max Planck Society.

Conflicts of interest

There are no conflicts to declare.

Notes and references

1 J. F. Lovell, C. S. Jin, E. Huynh, H. Jin, C. Kim, J. L. Rubinstein, W. C. Chan, W. Cao, L. V. Wang and G. Zheng, *Nat. Mater.*, 2011, **10**, 324–332.
2 X. Cai, D. Mao, C. Wang, D. Kong, X. Cheng and B. Liu, *Angew. Chem., Int. Ed.*, 2018, **57**, 16396–16400.
3 H. Park, W. Park and K. Na, *Biomaterials*, 2014, **35**, 7963–7969.
4 Y. Li, T. Y. Lin, Y. Luo, Q. Liu, W. Xiao, W. Guo, D. Lac, H. Zhang, C. Feng, S. Wachsmann-Hogiu, J. H. Walton, S. R. Cherry, D. J. Rowland, D. Kukis, C. Pan and K. S. Lam, *Nat. Commun.*, 2014, **5**, 4712.
5 G. Lan, K. Ni, S. S. Veroneau, X. Feng, G. T. Nash, T. Luo, Z. Xu and W. Lin, *J. Am. Chem. Soc.*, 2019, **141**, 4204–4208.
6 G. Lan, K. Ni, Z. Xu, S. S. Veroneau, Y. Song and W. Lin, *J. Am. Chem. Soc.*, 2018, **140**, 5670–5673.
7 K. Zhang, X. D. Meng, Y. Cao, Z. Yang, H. F. Dong, Y. D. Zhang, H. T. Lu, Z. J. Shi and X. J. Zhang, *Adv. Funct. Mater.*, 2018, **28**, 1804634.
8 Q. L. Wei, Y. Chen, X. B. Ma, J. F. Ji, Y. Qiao, B. Zhou, F. Ma, D. S. Ling, H. Zhang, M. Tian, J. Tian and M. Zhou, *Adv. Funct. Mater.*, 2018, **28**, 1704634.
9 J. Song, X. Yang, Z. Yang, L. Lin, Y. Liu, Z. Zhou, Z. Shen, G. Yu, Y. Dai, O. Jacobson, J. Munasinghe, B. Yung, G. J. Teng and X. Chen, *ACS Nano*, 2017, **11**, 6102–6113.
10 J. A. Hubbell and A. Chilkoti, *Science*, 2012, **337**, 303–305.
11 G. Song, L. Cheng, Y. Chao, K. Yang and Z. Liu, *Adv. Mater.*, 2017, **29**, 1700996.
12 N. J. Butcher, G. M. Mortimer and R. F. Minchin, *Nat. Nanotechnol.*, 2016, **11**, 310–311.
13 J. Xu, J. Bussiere, J. Yie, A. Sickmier, P. An, E. Belouski, S. Stanislaus and K. W. Walker, *Bioconjugate Chem.*, 2013, **24**, 915–925.
14 M. Liu, P. Johansen, F. Zabel, J. C. Leroux and M. A. Gauthier, *Nat. Commun.*, 2014, **5**, 5526.
15 L. Zhang, D. Shi, C. Shi, L. Dong, X. Li and M. Chen, *Macromol. Biosci.*, 2017, **17**, 1600522.
16 J. Zhao, Z. Qin, J. Wu, L. Li, Q. Jin and J. Ji, *Biomater. Sci.*, 2017, **6**, 200–206.
17 L. Li, Y. Song, J. L. He, M. Z. Zhang, J. Liu and P. H. Ni, *J. Mater. Chem. B*, 2019, **7**, 786–795.
18 S. Iwasaki, H. Kawasaki and Y. Iwasaki, *Langmuir*, 2019, **35**, 1749–1755.
19 Y. Tang, Y. Li, S. Li, H. Hu, Y. Wu, C. Xiao, Z. Chu, Z. Li and X. Yang, *Nanoscale*, 2019, **11**, 6217–6227.
20 K. Zhao, D. Li, W. Xu, J. Ding, W. Jiang, M. Li, C. Wang and X. Chen, *Biomaterials*, 2017, **116**, 82–94.
21 H. P. Li, Z. W. Zhou, F. R. Zhang, Y. X. Guo, X. Yang, H. L. Jiang, F. Tan, D. Oupicky and M. J. Sun, *Nano Res.*, 2018, **11**, 4627–4642.
22 H. Elzeny, F. Zhang, E. N. Ali, H. A. Fathi, S. Zhang, R. Li, M. A. El-Mokhtar, M. A. Hamad, K. L. Wooley and M. Elsabahy, *Drug Des., Dev. Ther.*, 2017, **11**, 483–496.
23 K. Hirota, T. Hristova, V. Mitova, T. Koda, M. Fushimi, M. Kuniya, K. Makino, H. Terada, R. Cherkezova, S. Yusa, N. Koseva and K. Troev, *Anticancer Res.*, 2016, **36**, 1613–1620.
24 R. Moriyama, Y. Iwasaki and D. Miyoshi, *J. Phys. Chem. B*, 2015, **119**, 11969–11977.
25 X. Liu, Y. Li, X. Tan, R. Rao, Y. Ren, L. Liu, X. Yang and W. Liu, *Biomaterials*, 2018, **157**, 136–148.
26 M. Yao, Y. Ma, H. Liu, M. I. Khan, S. Shen, S. Li, Y. Zhao, Y. Liu, G. Zhang, X. Li, F. Zhong, W. Jiang and Y. Wang, *Biomacromolecules*, 2018, **19**, 1130–1141.
27 K. N. Bauer, L. Liu, D. Andrienko, M. Wagner, E. K. Macdonald, M. P. Shaver and F. R. Wurm, *Macromolecules*, 2018, **51**, 1272–1279.
28 Y. P. Borguet, S. Khan, A. Noel, S. P. Gunsten, S. L. Brody, M. Elsabahy and K. L. Wooley, *Biomacromolecules*, 2018, **19**, 1212–1222.
29 F. Zhang, J. A. Smolen, S. Zhang, R. Li, P. N. Shah, S. Cho, H. Wang, J. E. Raymond, C. L. Cannon and K. L. Wooley, *Nanoscale*, 2015, **7**, 2265–2270.
30 P. Pei, C. Sun, W. Tao, J. Li, X. Yang and J. Wang, *Biomaterials*, 2019, **188**, 74–82.
31 H. Jin, M. Sun, L. Shi, X. Zhu, W. Huang and D. Yan, *Biomater. Sci.*, 2018, **6**, 1403–1413.
32 S. Schottler, G. Becker, S. Winzen, T. Steinbach, K. Mohr, K. Landfester, V. Mailander and F. R. Wurm, *Nat. Nanotechnol.*, 2016, **11**, 372–377.
33 C. Bernhard, K. N. Bauer, M. Bonn, F. R. Wurm and G. Gonella, *ACS Appl. Mater. Interfaces*, 2019, **11**, 1624–1629.
34 L. Huang, Z. Li, Y. Zhao, J. Yang, Y. Yang, A. I. Pendharkar, Y. Zhang, S. Kelmar, L. Chen, W. Wu, J. Zhao and G. Han, *Adv. Mater.*, 2017, **29**, 1604789.
35 M. Huo, L. Wang, Y. Chen and J. Shi, *Nat. Commun.*, 2017, **8**, 357.
36 G. X. Liu, Y. M. Zhang, X. F. Xu, L. Zhang, Q. L. Yu, Q. Zhao, C. Y. Zhao and Y. Liu, *Adv. Opt. Mater.*, 2017, **5**, 1700770.

